Available online at www.sciencedirect.com
SCIENCE DIRECT®
International Journal of Thermal Sciences 42 (2003) 677–686
International Journal of Thermal Sciences
www.elsevier.com/locate/ijts

Heat transfer from a continuous liquid to an evaporating drop: a numerical analysis

Frank Dammel *, Hans Beer

Institut für Technische Thermodynamik, Technische Universität Darmstadt, 64287 Darmstadt, Germany

Received 19 April 2002; accepted 8 August 2002

Abstract

Heat transfer from a continuous liquid to a drop of a second immiscible liquid, which rises due to buoyancy and simultaneously evaporates in direct contact to the continuous liquid, is examined numerically. The finite element method in a pure Lagrangian description is applied. The shape of the interfaces has not to be prescribed and the full Navier–Stokes equations are solved. Calculations are performed for a furan drop and for a *n*-pentane drop evaporating in aqueous glycerol.

In the initial stage, when the rising velocity and the vapour fraction of the compound drop are small, heat transfer by conduction dominates. With increasing time convective heat transfer becomes more important, even in the liquid of the dispersed component where a vortex is generated. Most of the heat transfer from the continuous to the dispersed component takes place in a small region at the contact circle of the three phases. Because of convection in the liquid of the compound drop, the heat flux at the internal liquid–vapour interface of the dispersed component and thus the evaporation is distributed more uniformly. Even though the thermal resistance of the drop's liquid is higher than that of the continuous liquid, the share of neither liquid on the total resistance can be neglected.

Keywords: Compound drop; Direct-contact evaporation; Heat transfer; Free interface flow; Finite element method; Lagrangian description

1. Introduction

For some applications it can be advantageous to use direct contact heat exchangers instead of conventional surface-type ones. Since there are no separating walls and the heat transfer area is larger for a given volume, high heat fluxes are achieved at low temperature differences and small pressure drops. Direct contact heat transfer takes place between two process streams which are inevitably at the same pressure. Further restrictions are that the two fluids must not react chemically and should be immiscible. Different types of direct contact heat exchangers are described in [1].

In many cases the heat transfer takes place between a liquid, the continuous component, and the drops of a second liquid, the dispersed component, which rise due to buoyancy. If the temperature of the continuous liquid is above the saturation temperature of the dispersed component, the drops evaporate while rising and form continuously growing compound drops. In this case, shown schematically in Fig. 1, the dispersed component stores the heat transferred by the surrounding liquid as latent heat without a significant increase in temperature. Depending primarily on the interfacial tensions, different configurations are possible [2]. The most common one is the "partially engulfed configuration" shown in Fig. 2, where each of the three phases is in contact with the other two. This figure includes also the numbering of the phases and, derived from it, the naming of the interfaces. An often used quantity to describe the progress of evaporation is the vaporisation ratio ξ. It is defined as the ratio of the vapour mass to the total mass of the compound drop.

$$\xi = \frac{m_{\mathrm{dc,v}}}{m_{\mathrm{dc}}} = \frac{m_{\mathrm{dc,v}}}{m_{\mathrm{dc,l}} + m_{\mathrm{dc,v}}} \tag{1}$$

A general overview of direct contact processes with moving drops is given by Ayyaswamy [3]. Industrial applications are, for example, desalination of seawater [4], waste heat recovery and emergency cooling of chemical reactors [5]. Furthermore, direct contact evaporation may be used in geothermal [6], ocean-thermal [7] or solar pond [8] power plants, where electricity is generated from low or moderate temperature heat sources.

For the design and the layout of these heat exchangers models are needed that describe the influence of the different parameters on the evaporation of drop swarms. In general,

* Corresponding author.
E-mail addresses: dammel@ttd.tu-darmstadt.de (F. Dammel), beer@ttd.tu-darmstadt.de (H. Beer).

1290-0729/03/$ – see front matter
doi:10.1016/S1290-0729(03)00033-4

Nomenclature

A	area
c_p	specific heat capacity
D	diameter
f_m	artificial mass source
$\boldsymbol{f}$	vector of mass forces
g	gravitational acceleration
Δh_{lv}	evaporation enthalpy
H	ascent height
$\boldsymbol{I}$	unity matrix
l	length of interface
m	mass
$\dot{m}_{\mathrm{lv}}$	mass evaporation rate
$\boldsymbol{n}$	unit normal vector
p	pressure
$\boldsymbol{q}$	vector of heat flux
$\bar{q}$	average heat flux
$\dot{Q}$	rate of heat flow
r	radial coordinate
R	Radius of contact circle
s	coordinate along interface
t	time
T	temperature
$\boldsymbol{\mathcal{T}}$	stress vector
$\boldsymbol{u}$	velocity vector
U	velocity of rise
V	volume
W	thermal resistance
z	axial coordinate

Greek symbols

γ	interfacial tension
δ	interface angle
θ	contact angle
κ	curvature
λ	thermal conductivity
μ	dynamic viscosity
ξ	vaporisation mass ratio
ρ	density
$\boldsymbol{\sigma}$	stress tensor
ϕ	angular coordinate

Subscripts

cc	continuous component
dc	dispersed component
env	environment
l	liquid
n	normal component
r	radial component
s	value at saturation
t	tangential component
v	vapour
z	axial component
ϕ	angular component
0	initial value
1/2/3	phase 1/2/3
12/13/23	interface 1-2/1-3/2-3
∞	far field value

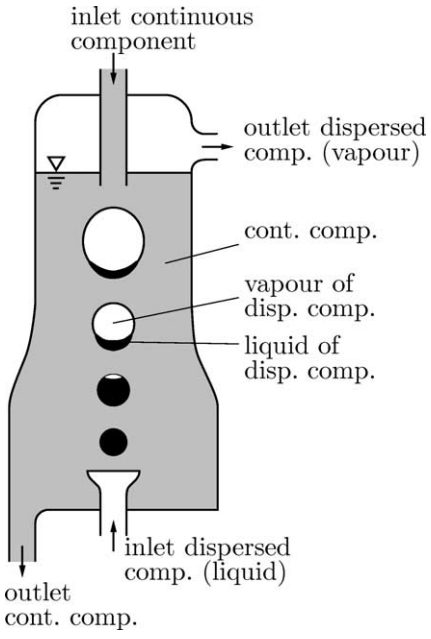

Fig. 1. Schematic sketch of a direct-contact heat exchanger with evaporation.

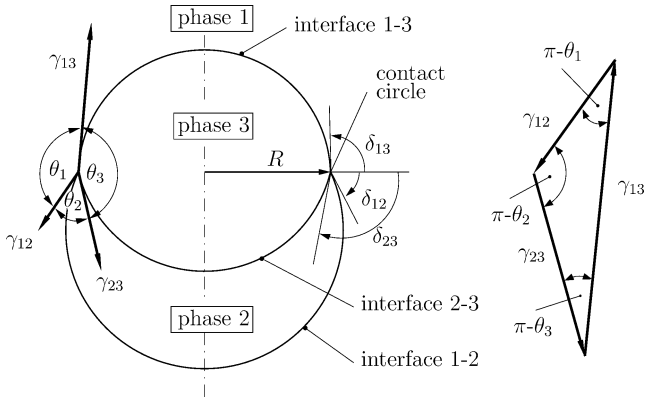

Fig. 2. Partially engulfed configuration of a compound drop and force balance of interfacial tensions in the limit of static equilibrium.

breakage of drops and drop interactions cannot be neglected. Because of the motion of the interfaces between the phases, the heat transfer area may change with time and can hardly be determined. Therefore, volumetric heat transfer coefficients are used. They and other important characteristic quantities, such as the evaporation height, are calculated by

applying single drop correlations, which are modified and extended for the case of an evaporating drop swarm [5,9,10].

Beginning in the 1960s the direct-contact evaporation of single drops has been studied extensively. In experimental investigations [4,11,12] rather global results were obtained, such as rising velocities, times for complete evaporation, optimum height and overall heat transfer coefficients. It was found that in low viscous continuous phases the compound drops undergo shape oscillations and rise in a zig–zag path [11,12]. This causes the liquid of the two-phase drops to slosh from side to side. Such oscillations were not observed when continuous components with higher viscosities were used [11,13,14]. The reason is presumably vortex shedding in the wake [12].

In analytical and numerical studies done so far, usually the shape of the compound drop is approximated by a sphere [4,13,14] or an ellipsoid and Stokes [13,14] or potential flow [4] is assumed. Vuong and Sadhal [15,16] computed the evaporation of a pentane drop in glycerol. They assumed that the shape is solely determined by the interfacial tensions and solved the flow field analytically in the limit of Stokes flow. Afterwards they calculated the temperature distribution and the evaporation rates numerically. Wohak and Beer [17] tried to simulate the problem numerically without any restrictions on the shape. They solved the full Navier–Stokes equations on a fixed grid in an Eulerian description. To track the interfaces the volume of fluid method (VOF) was applied. It turned out, however, that it was not possible to resolve the course of the interfaces with an accuracy necessary to calculate temperature gradients and evaporation rates properly. The conclusion seems to be that a boundary-fitted method, in which the interfaces always coincide with grid lines, is more suitable.

Despite the large number of investigations carried out so far, the direct contact evaporation of a rising drop in another liquid is still not fully understood. The purpose of this study is the development of a numerical procedure without prescribing the shape of the compound drop and without severely simplifying the equations of motion. Following the experiments of Tochitani et al. [13,14], the developed code is evaluated on the basis of two calculations. Additionally, the numerical results enable a more detailed analysis of the heat transfer mechanism.

2. Procedure

2.1. Physical model

In contrast to most former theoretical investigations, in the present study the shape of the compound drop is not prescribed and the Navier–Stokes equations are not simplified with the Stokes or the potential theory. However, the problem under consideration is characterized by the interaction of several physical phenomena. To enable the numerical simulation of this complex process, the prescription of some simplifying assumptions, which are stated in this section, is unavoidable.

At the beginning a liquid drop with a small vapour nucleus at its front, the dispersed component, is at rest in another liquid, the continuous component. Both liquids are incompressible, obey the Newtonian material law and have constant properties. Initially, the shape of the three interfaces is solely determined by the interfacial tensions and each of the two components has a locally constant temperature. While the compound drop possesses the saturation temperature corresponding to the hydrostatic pressure, the temperature of the surrounding liquid is above that value.

Due to its lower specific weight, the compound drop starts to rise. To restrict the calculations to the two-dimensional case, it is assumed that the rise is linear upwards with axisymmetric deformations in laminar flow. This is true for small and medium Reynolds numbers and thus for rather viscous continuous liquids. Since the viscosity of the vapour is much smaller than the respective values of the two liquids, shear stresses at the interfaces 1-3 and 2-3 (see Fig. 2) are neglected. Each of the three interfaces is infinitely thin and has a constant value of interfacial tension. Neglecting the temperature dependence of the interfacial tensions and thus Marangoni convection seems to be justified, because the temperature differences in the cases under consideration are small.

Simultaneously to its rise heat is transferred to the compound drop from the surrounding liquid. The thermal conductivity of the dispersed component's vapour is much smaller than that of its liquid. Therefore, only a negligible fraction of the total heat is transferred over interface 1-3 directly to the vapour. At the internal liquid–vapour interface 2-3 heat transfer controlled evaporation takes place, and this interface is always at saturation temperature. While the hydrostatic pressure has to be considered, the influence of the interfacial curvature on the saturation temperature is small and can be neglected [18].

2.2. Governing equations

2.2.1. Conservation equations

Considering the assumptions of the preceding section, the physical model is described by the conservation equations of mass (2), momentum (3) and energy (4) for incompressible fluids with constant material properties and neglected viscous dissipation.

$$\nabla \cdot \boldsymbol{u} = f_m \tag{2}$$

$$\rho \frac{\mathrm{D}\boldsymbol{u}}{\mathrm{D}t} = \nabla \cdot \boldsymbol{\sigma} + \rho \boldsymbol{f} \tag{3}$$

$$\rho c_p \frac{\mathrm{D}T}{\mathrm{D}t} = -\nabla \cdot \boldsymbol{q} \tag{4}$$

The fluids are Newtonian (5) and obey the Fourier heat conduction law (6).

$$\boldsymbol{\sigma} = -p\boldsymbol{I} + \mu\left[(\nabla \boldsymbol{u}) + (\nabla \boldsymbol{u})^T\right] \tag{5}$$

$$\boldsymbol{q} = -\lambda \nabla T \tag{6}$$

Specified for axisymmetric cylindrical coordinates (r, ϕ, z) with vanishing angular velocity ($u_\phi \equiv 0$) and gravity g acting in negative z-direction, the above equations read:

$$\frac{\partial u_r}{\partial r} + \frac{u_r}{r} + \frac{\partial u_z}{\partial z} = f_m \tag{7}$$

$$\begin{aligned} \rho \frac{\mathrm{D}u_r}{\mathrm{D}t} &= \frac{1}{r}\frac{\partial}{\partial r}(r\sigma_{rr}) + \frac{\partial \sigma_{rz}}{\partial z} - \frac{\sigma_{\phi\phi}}{r} \\ \rho \frac{\mathrm{D}u_z}{\mathrm{D}t} &= \frac{1}{r}\frac{\partial}{\partial r}(r\sigma_{rz}) + \frac{\partial \sigma_{zz}}{\partial z} + \rho g \end{aligned} \tag{8}$$

$$\rho c_p \frac{\mathrm{D}T}{\mathrm{D}t} = -\frac{1}{r}\frac{\partial}{\partial r}(r q_r) - \frac{\partial q_z}{\partial z} \tag{9}$$

They contain the following components of the stress tensor and the vector of heat flux:

$$\begin{aligned} \sigma_{rr} &= -p + 2\mu \frac{\partial u_r}{\partial r}, & \sigma_{\phi\phi} &= -p + 2\mu \frac{u_r}{r} \\ \sigma_{zz} &= -p + 2\mu \frac{\partial u_z}{\partial z}, & \sigma_{rz} &= \mu\left(\frac{\partial u_r}{\partial z} + \frac{\partial u_z}{\partial r}\right) \end{aligned} \tag{10}$$

$$q_r = -\lambda \frac{\partial T}{\partial r}, \qquad q_z = -\lambda \frac{\partial T}{\partial z} \tag{11}$$

2.2.2. Initial configuration

To calculate the initial contact angles the cosine law is applied to the triangle formed by the three vectors of the interfacial tensions (see right side of Fig. 2).

$$\theta_1 = \arccos\left(\frac{\gamma_{23}^2 - \gamma_{12}^2 - \gamma_{13}^2}{2\gamma_{12}\gamma_{13}}\right) \tag{12}$$

$$\theta_2 = \arccos\left(\frac{\gamma_{13}^2 - \gamma_{12}^2 - \gamma_{23}^2}{2\gamma_{12}\gamma_{23}}\right) \tag{13}$$

$$\theta_3 = \arccos\left(\frac{\gamma_{12}^2 - \gamma_{13}^2 - \gamma_{23}^2}{2\gamma_{13}\gamma_{23}}\right) = 2\pi - \theta_1 - \theta_2 \tag{14}$$

For a given total mass m_{dc} of the dispersed component and a given initial vaporisation mass ratio ξ_0 the initial shape of the compound drop can be determined. For that purpose the radius R of the three phase contact circle and the tangential angles δ_{12}, δ_{13} and δ_{23} of the interfaces with a horizontal have to be calculated.

$$\begin{aligned} V_{\mathrm{dc,l}} &= \frac{(1-\xi_0)m_{\mathrm{dc}}}{\rho_{\mathrm{dc,l}}} \\ &= \frac{\pi}{3}R^3\left[\frac{(1+\cos\delta_{12})^2(2-\cos\delta_{12})}{\sin^3\delta_{12}} - \frac{(1+\cos\delta_{23})^2(2-\cos\delta_{23})}{\sin^3\delta_{23}}\right] \end{aligned} \tag{15}$$

$$\begin{aligned} V_{\mathrm{dc,v}} &= \frac{\xi_0 m_{\mathrm{dc}}}{\rho_{\mathrm{dc,v}}} \\ &= \frac{\pi}{3}R^3\left[\frac{(1+\cos\delta_{13})^2(2-\cos\delta_{13})}{\sin^3\delta_{13}} + \frac{(1+\cos\delta_{23})^2(2-\cos\delta_{23})}{\sin^3\delta_{23}}\right] \end{aligned} \tag{16}$$

The tangential angles are connected with the contact angles:

$$\delta_{13} = \theta_1 - \delta_{12} \tag{17}$$

$$\delta_{23} = \theta_2 + \delta_{12} \tag{18}$$

2.2.3. Boundary and transition conditions

The boundary and transition conditions are summarized in Fig. 3. The outer boundary of the computational domain, which is divided into parts I to VI, does not enclose the vapour of the dispersed component. The interactions between the vapour and the two liquids are considered by appropriate boundary conditions on parts V and VI. Curve VII, the liquid–liquid interface 1-2, is not part of the boundary but inside the computational domain. To consider the interfacial tension a transition condition has to be applied on that curve.

For the fluid dynamics part either the velocity components u_r and u_z or the tangential and normal components of the surface stress vector $\mathcal{T}_t$ and $\mathcal{T}_n$ are specified. In the same way, for the energy equation either the temperature T or the heat flux normal to the interface q_n is prescribed.

Parts I and II of the boundary represent bottom and side wall of the container Tochitani et al. [13,14] used in their experiments. There the no-slip condition is imposed on the velocity and the temperature has its far field value. The top of the container, part III, is a free surface on which the environmental pressure acts as the normal component of the stress vector. Part IV is the line of symmetry with the respective boundary conditions. Curves V to VII represent the interfaces between the three phases. Each of the interfaces possesses a constant value of the interfacial tension which causes a normal stress that depends on the local curvature κ.

$$\mathcal{T}_n(s,t) = \gamma\kappa \tag{19}$$

When the shape of an interface is given in cylindrical coordinates by $z = f(r)$, the equation for the curvature reads as

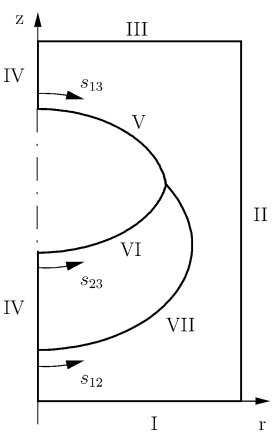

Boundary conditions	
I	$u_r = 0;\ u_z = 0;$ $T = T_\infty$
II	$u_r = 0;\ u_z = 0;$ $T = T_\infty$
III	$\mathcal{T}_t = 0;\ \mathcal{T}_n = -p_{\mathrm{env}};$ $T = T_\infty$
IV	$u_r = 0;\ \partial u_z/\partial r = 0;$ $\partial T/\partial r = 0$
V	$\mathcal{T}_t = 0;\ \mathcal{T}_n = \gamma_{13}\kappa(s_{13}) - p_{\mathrm{dc,v}};$ $q_n = 0$
VI	$\mathcal{T}_t = 0;\ \mathcal{T}_n = \gamma_{23}\kappa(s_{23}) - p_{\mathrm{dc,v}};$ $T = T_{\mathrm{s}}(z)$
Transition condition	
VII	$\Delta\mathcal{T}_n = \gamma_{12}\kappa(s_{12})$

Fig. 3. Boundary and interfacial conditions (not true to scale).

follows:

$$\kappa = \frac{f''}{[1+(f')^2]^{3/2}} - \frac{f'}{r[1+(f')^2]^{1/2}} \tag{20}$$

At curves V and VI besides the influence of the interfacial tension on the normal component of the stress vector, the pressure $p_{\mathrm{dc,v}}$ of the dispersed component's vapour has to be considered.

At interface 2-3 (part VI of the boundary), which is always at the saturation temperature corresponding to the hydrostatic pressure, the mass evaporation rate has to be calculated.

$$\dot{m}_{\mathrm{lv}} = -2\pi \frac{\lambda_2}{\Delta h_{\mathrm{lv}}} \int_0^{l_{23}} \left(\frac{\partial T}{\partial r} n_r + \frac{\partial T}{\partial z} n_z \right) r \, \mathrm{d}s_{23} \tag{21}$$

2.3. Numerical method

For the spatial discretisation of the governing system of differential equations the finite element method is applied. This method is especially suitable for problems including curved boundaries or interfaces. In computational fluid dynamics usually the Eulerian description is chosen, where the mesh is stationary. If a transient problem with moving interfaces is treated, an additional component is necessary to trace the motion of the interfaces. Wohak [19], who applied the volume of fluid (VOF) method for that purpose, concludes that such a procedure is not very suitable for the special case of a rising liquid drop evaporating in direct contact with another liquid. Therefore, here the Lagrangian description is preferred, where the mesh moves with the material velocity of the fluid. Advantages are that the interfaces always coincide with element sides and that the nonlinear convection terms are absent. However, the moving mesh becomes more and more distorted and many remeshing steps with adjacent data transfer from the old to the new mesh are necessary to prevent the mesh from being destroyed.

The so-called Q2/P1–Crouzeix–Raviart element [20] with 9 nodes is used. It interpolates shape, velocity and temperature bi-quadratically and the pressure linearly. Since the pressure interpolation is discontinuous, it is possible to consider the pressure steps across interfaces caused by the interfacial tensions. The most important advantage of this element is, however, that its volume changes only very little in time, a crucial feature when a Lagrangian description is used.

The temporal development of the vapour mass is calculated by summing up the initial vapour mass and the evaporation rates of the single time steps. To ensure that the vapour takes up the volume equivalent to its mass, the normal stress boundary condition at the interfaces between the vapour and the two liquids is adjusted appropriately. Physically, this means that the vapour pressure is slightly increased when its volume is too small and, in the reverse case, decreased when its volume is too large.

The mass of the compound drop's liquid is the difference between the constant total mass of the dispersed component and the vapour mass. Its reduction due to evaporation and small errors caused by the remeshing steps are considered by means of the artificial mass source, which is evenly distributed over the liquid of the compound drop.

A more detailed description of the numerical method can be found in [18,21].

3. Performed calculations

With the developed simulation code it is only possible to carry out calculations for systems that possess a rather viscous continuous component. Otherwise a two-dimensional description is not justified, because then the compound drop would undergo shape oscillations while rising in a zig–zag path. This has significant influence on the heat transfer but cannot be considered in the numerical simulation. Therefore, following the experiments of Tochitani et al. [13,14], two calculations were executed that fulfil this limiting condition. Firstly, a furan drop with initial diameter $D_0 = 1.36$ mm evaporates in aqueous glycerol with a glycerol mass fraction of 96.1%, and secondly, a *n*-pentane drop with initial diameter $D_0 = 1.42$ mm evaporates also in aqueous glycerol, but in this case the glycerol fraction is 98.3%. The nominal temperature difference is $T_\infty - T_\mathrm{s} = 3.1$ K, where T_s is, as set in [13,14], the saturation temperature of the dispersed component at a height of 96 mm in the experimental column. Since the total height of the column is 580 mm, the actual superheating is increasing during an experiment from about 2.8 K at the bottom to 4 K at the top. Similar to the experiment, where the drop initially contains a tiny artificial air bubble nucleus, the numerical simulation starts with a compound drop that has a vaporisation ratio $\xi_0 = 0.01\%$. As in the experiments, the calculations are continued until vaporisation mass ratios of $\xi \approx 19\%$ are reached.

Mori et al. [22] measured the interfacial tensions for several systems of two liquids and their common, saturated vapour by use of the pendant-drop method. Among these systems were furan-glycerol and *n*-pentane–glycerol. Own measurements, carried out with the Wilhelmy-plate method, showed that the use of pure glycerol instead of aqueous glycerol with a small water fraction has no significant influence on the interfacial tensions. Therefore, the values used in the calculations, compiled in Table 1, are interpolated from the temperature dependent values of high accuracy in [22].

All other material properties are given in Table 2. The values for liquid furan and liquid *n*-pentane are determined at their saturation temperatures of 31.5 °C and 36.1 °C, respectively, corresponding to a pressure of 1013 mbar. For the densities of their vapours the average hydrostatic pressure is taken into account. The values of aqueous glycerol belong to the respective far field temperature T_∞.

The liquid furan is discretized with 55 elements and the aqueous glycerol with 206 resulting in 4158 degrees of

Table 1
Interfacial tensions

	γ_{12} [mN·m^{-1}]	γ_{23} [mN·m^{-1}]	γ_{13} [mN·m^{-1}]
Furan system	15.06	22.17	36.45
n-pentane system	27.74	14.39	41.58

freedom of which 244 are fixed by essential boundary conditions. Since a time step size between 10^{-5} and 10^{-4} s and about 10 iterations per time step are necessary to achieve convergence, the required computational times are rather long.

4. Results

4.1. Shapes and motion

Fig. 4 shows the time history of the vaporisation ratio for both systems. After about 5.2 s for the *n*-pentane and 6.5 s for the furan system the final vaporisation ratio $\xi \approx 19\%$ is reached. The vaporisation ratio of the *n*-pentane drop increases faster mainly because of its smaller total mass and its smaller evaporation enthalpie. Especially at the beginning the gradient of both curves and thus the evaporating mass per unit time is increasing with time.

The final values of the velocity of rise, shown in Fig. 5, are 90 mm·s^{-1} for the furan and 80 mm·s^{-1} for the *n*-pentane drop. The furan drop rises faster, because for equal vaporisation ratios its volume is larger than that of the *n*-pentane drop. Experimental comparison values are only available for the *n*-pentane system, where good agreement can be found. Fig. 6, which depicts the vaporisation ratio over the ascent height, includes experimental results [23] for both systems. It seems as if an imagined curve through the experimental data points (not included in Fig. 6) would cut the abscissa a little bit right from the origin. The cause for it is the fact that in the experiments the drops have an initial temperature that is slightly below the saturation temperature. For this reason, at the very beginning the heat transferred from the continuous component warms up the drop's liquid without a significant increase of the vaporisation ratio. Analogously to the time history, the vaporisation ratio of the *n*-pentane drop is higher than that of the furan drop for the same ascent height. Qualitatively, the experimental values show the same behaviour. However, the differences are more pronounced: While the experimental data points for the furan system are slightly below the numerically calculated curve, those for the *n*-pentane system are considerably above. Since the velocities of rise are in good agreement, this means that the *n*-pentane drop evaporates faster in the experiment than in the simulation.

Fig. 7 depicts the numerically calculated shapes for several vaporisation ratios ξ of the *n*-pentane drop in comparison with the photographs [23] taken by Tochitani et al. in their experiments. Additionally, the figure contains on the left side the static contours, which would appear if only interfacial forces would act. The differences between the actual contours and the static contours may be interpreted

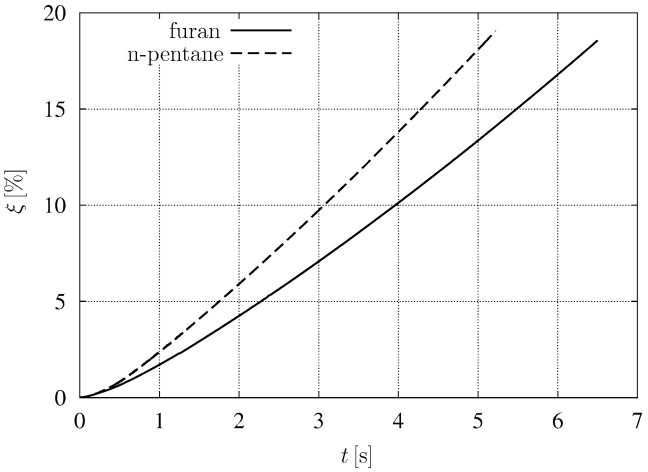

Fig. 4. Time history of the vaporisation ratio.

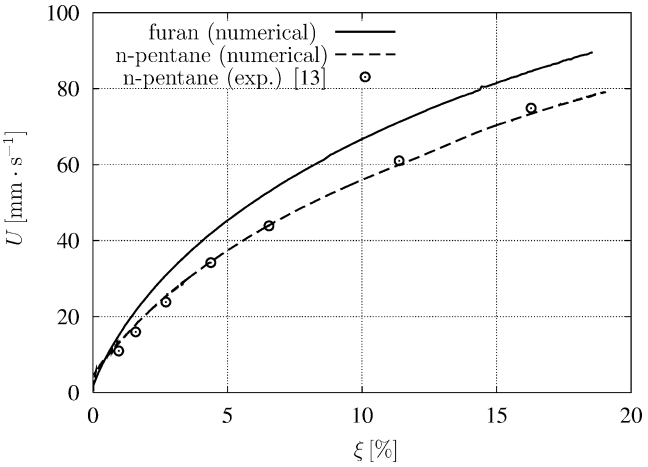

Fig. 5. Velocity of rise.

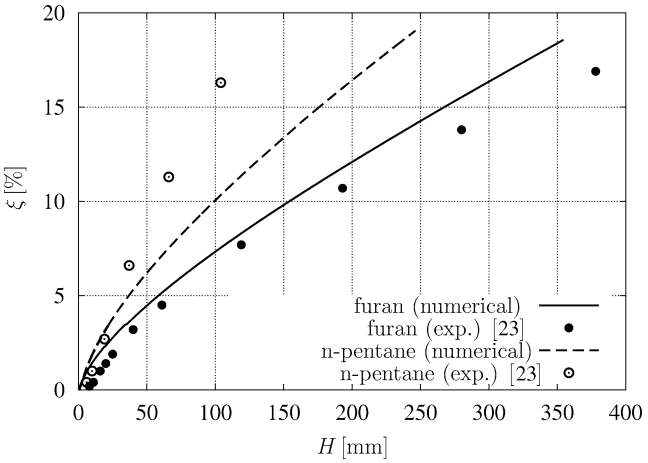

Fig. 6. Vaporisation ratio versus ascent height.

Table 2
Material properties

	ρ [kg·m^{-3}]	μ [mN·s·m^{-2}]	λ [W·m^{-1}·K^{-1}]	c_p [J·kg^{-1}·K^{-1}]	Δh_{lv} [kJ·kg^{-1}]
Aqueous glycerol (96.1 mass% glyc.)	1240	220	0.299	2510	
Furan liquid	922	0.34	0.143	1710	
Furan vapour	2.9				400
Aqueous glycerol (98.3 mass% glyc.)	1245	220	0.294	2510	
n-pentane liquid	610	0.196	0.107	2340	
n-pentane vapour	3.0				358

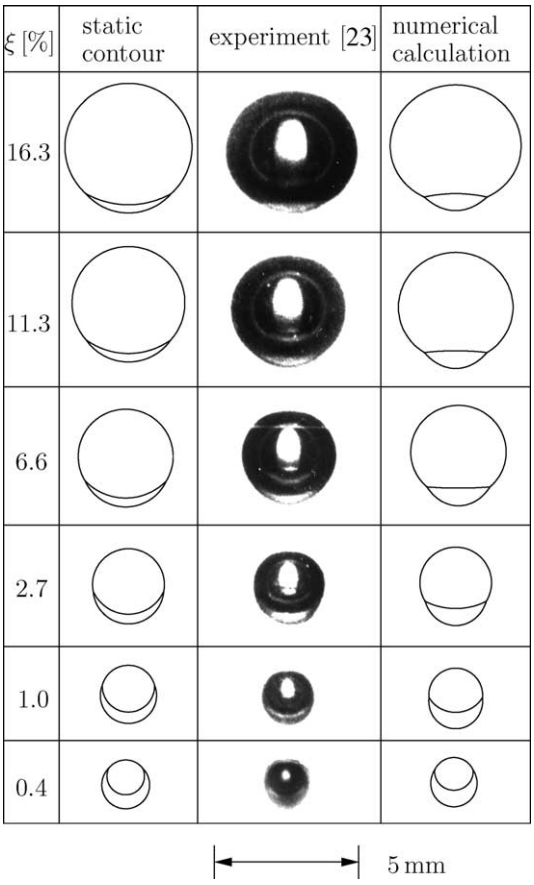

Fig. 7. Comparison of contours for the evaporating *n*-pentane drop.

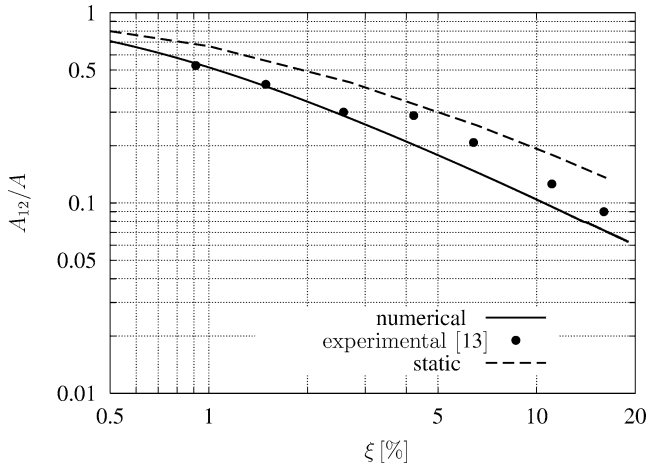

Fig. 8. Area ratio of the *n*-pentane drop ($A = A_{12} + A_{13}$).

as consequence of the additionally acting inertia, pressure, friction and gravity forces.

In the static equilibrium the opening angle of the drop's liquid at the contact circle (θ_2 in Fig. 2) is small, because the sum of the interfacial tensions γ_{12} and γ_{23} exceeds γ_{13} only slightly. Due to the shear stress at the liquid–liquid interface, which is taken into account additionally in the numerical calculation, the two points representing the contact circle in the vertical cut through the middle of the compound drop are moved towards the bottom of the drop. The angle θ_2 is increased and, in contrast to the static shapes, the curvature of the internal liquid–vapour interface 2-3 changes from concave to convex for higher vaporisation ratios.

For small vaporisation ratios the outer contours of the numerical shapes are in good agreement with the photographs. For larger vaporisation ratios, however, the experimental shapes are somewhere between static and numerically calculated shapes. The internal liquid–vapour interface of the compound drop is hardly visible on the photographs, and, because of effects like refraction and dispersion on the vaulted interfaces, the alleged shape on the photographs presumably does not match exactly the real one.

Experimental and numerically calculated shapes can also be compared by the areas of the interfaces. However, experimental comparative values are only available for the ratio of the liquid–liquid interface's area A_{12} to the total outer area of the compound drop $A = A_{12} + A_{13}$. Fig. 8 shows this ratio as a function of the vaporisation ratio for the *n*-pentane drop. Additionally, it contains the values for a static compound drop. The first three experimental data points coincide with the numerical curve, the others are in between the numerical and the static curve. The deformation of the compound drop relative to the static shape seems to be smaller in the experiment than in the numerical simulation. The most likely reason is discussed in the following paragraph.

In experiments it is commonly observed that smaller drops and bubbles, which rise due to buoyancy in a continuous liquid, tend to behave like rigid particles rather than

like fluid particles with free interfaces and that internal circulation is virtually absent. The most reasonable explanation is that surface-active substances accumulate at the interface and thereby reduce the interfacial tension [24]. Due to the ascent, these substances are swept to the rear, leaving the frontal region relatively uncontaminated. This concentration gradient causes a gradient of interfacial tension tending to immobilize all of the interface or a portion of it at the rear (stagnant cap). Possibly present surface-active substances in the experiments of Tochitani et al. could have mainly affected the liquid–liquid interface at the rear of the compound drop, where a tangential gradient of the interfacial tension could have retarded the motion of the interface and thus reduced the deformation. In the numerical simulation each interface possesses a constant interfacial tension and the mentioned effect is not considered.

4.2. Heat transfer

Fig. 9 shows the time history of the rates of heat flow $\dot{Q}_{12}$ and $\dot{Q}_{23}$ at interfaces 1-2 and 2-3, respectively, for the n-pentane system. The initial temperature distribution has a discontinuity at the liquid–liquid interface, where, at least in the physical model, the temperature changes abruptly from the far field temperature T_∞ to the saturation temperature T_s of the dispersed component. Therefore, the rate of heat flow $\dot{Q}_{12}$ is very high at the beginning, but decreases rapidly as the temperature gradient is reduced. In contrast, there is no initial temperature gradient at the internal interface 2-3 and consequently, the rate of heat flow $\dot{Q}_{23}$ starts at zero. Based on the area A of the total outer surface of the compound drop, this heat flux brings about heat transfer coefficients between 200 and 300 $\mathrm{W{\cdot}m^{-2}{\cdot}K^{-1}}$ for $\xi < 2\%$. For larger vaporisation ratios the influence of the increasing area A on the heat transfer coefficients exceeds that of the also increasing heat flux and thus the heat transfer coefficient decreases.

The difference between $\dot{Q}_{12}$ and $\dot{Q}_{23}$, present until a time of approximately 1.3 s is reached, heats up the compound drop's liquid. After that time the two curves nearly coincide and the heat transfer may be considered as quasi steady. Then the total rate of heat flow transferred can be expressed with the aid of the thermal resistance W.

$$\dot{Q}_{12} \approx \dot{Q}_{23} \approx \dot{Q} = \frac{T_\infty - T_s}{W} \tag{22}$$

The total thermal resistance may be subdivided into the shares W_{cc} of the continuous and W_{dc} of the dispersed component. Fig. 10 shows the time history, both for the total resistance and its two portions. Within the range depicted the values change hardly and the fraction of the dispersed component's resistance on the total resistance is approximately three quarters. The question, if the resistance of one of the two components can be neglected, is discussed controversially in the literature. At least for the system under consideration in the present work, the contribution of neither component should be neglected.

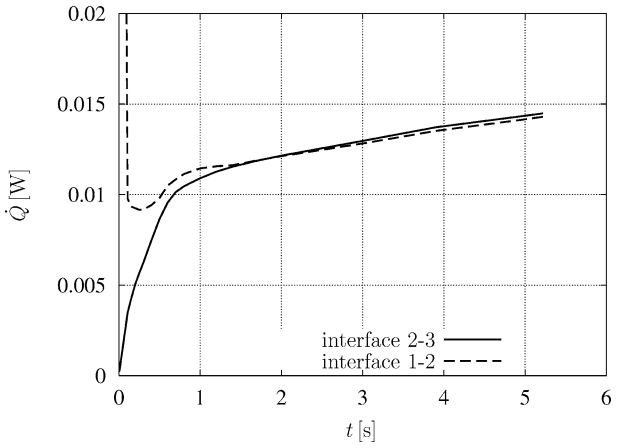

Fig. 9. History of the rates of heat flow (n-pentane system).

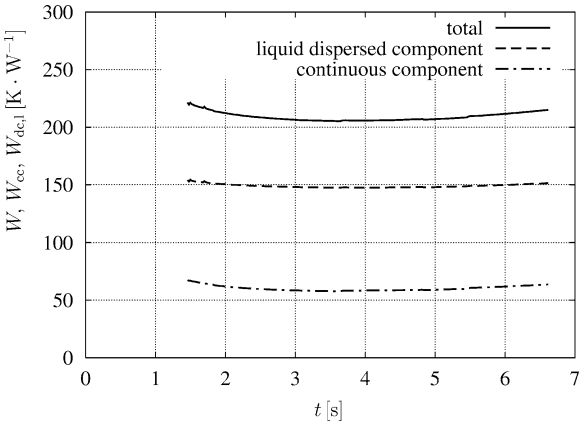

Fig. 10. History of thermal resistances (furan system).

The numerical simulation enables a more detailed analysis of the heat transfer mechanism than possible with experiments alone. For this purpose Figs. 11 and 12 show streamlines and isotherms for three different vaporisation ratios of the n-pentane compound drop. The streamlines were calculated using the rear stagnation point velocity as reference. When the drop is initially immersed into the hotter continuous component, a large temperature gradient is present at the liquid–liquid interface. During the early stage, represented by $\xi = 0.2\%$ in the figures, all velocities are small and conduction heat transfer dominates over convection. Apart from a small region close to the contact circle of the three interfaces, the isotherms evolve nearly parallel to interface 1-2. The smallest overall thermal resistance occurs in the vicinity of the three-phase contact circle, where only a thin, wedge-shaped body of liquid n-pentane separates T_s and T_∞. Therefore, in this region, even at the very beginning, heat transferred by pure conduction reaches interface 2-3, where evaporation commences immediately.

As the rising velocity increases, convection becomes more and more pronounced. Fig. 11 shows that a vortex is stimulated in the liquid of the compound drop by interfacial shear stress. Looking at the isotherms for the higher vaporisation ratios, they obviously lost their appearance typical

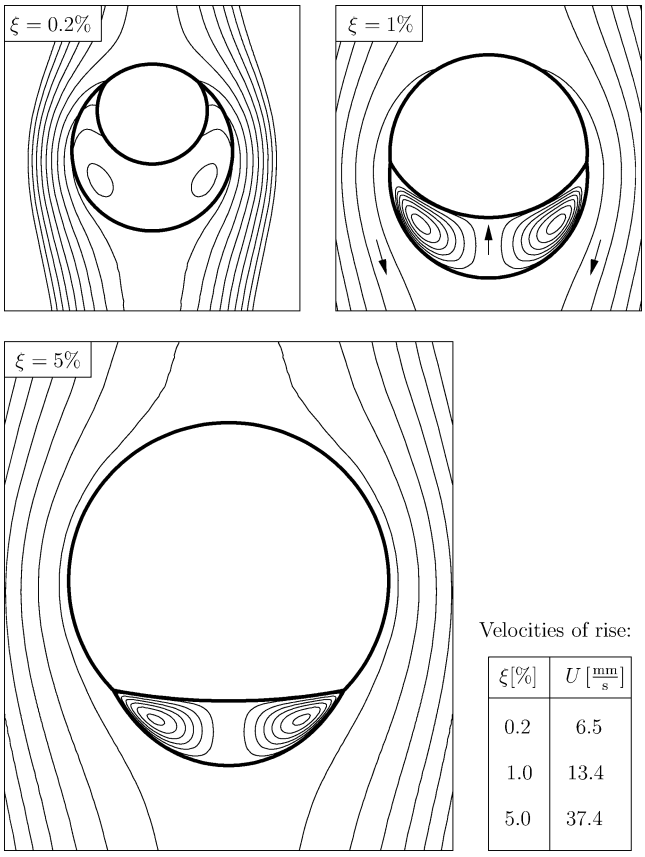

Velocities of rise:

ξ[%]	$U\,[\frac{\text{mm}}{\text{s}}]$
0.2	6.5
1.0	13.4
5.0	37.4

Fig. 11. Streamlines (n-pentane system).

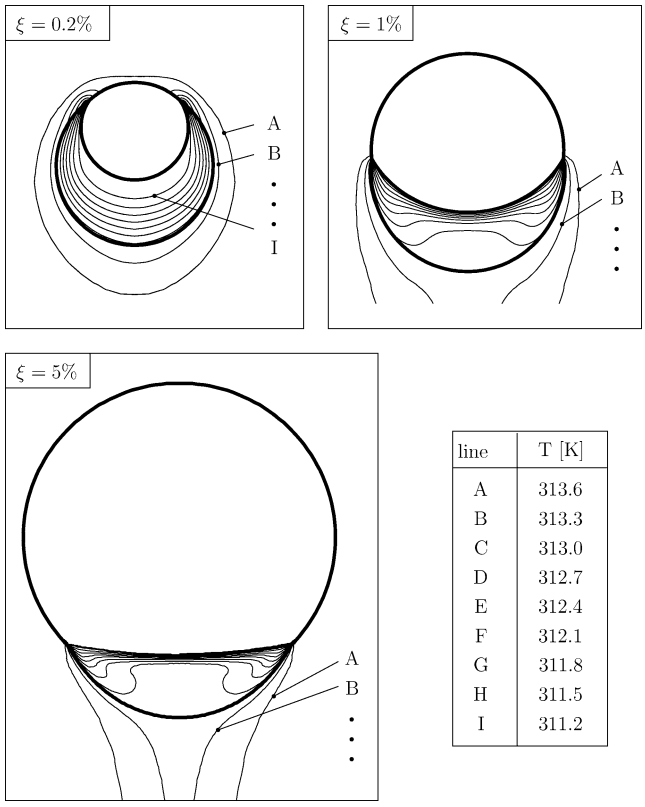

line	T [K]
A	313.6
B	313.3
C	313.0
D	312.7
E	312.4
F	312.1
G	311.8
H	311.5
I	311.2

Fig. 12. Isotherms (n-pentane system, $T_\infty = 313.7$ K).

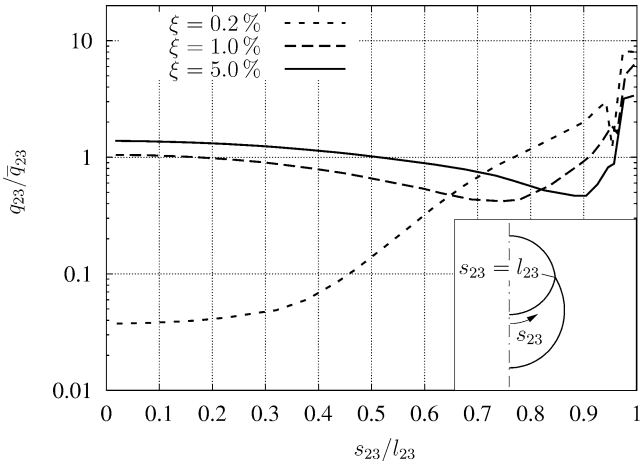

Fig. 13. Distribution of the heat flux (rate of heat flow per unit area) along the internal liquid–vapour interface of the n-pentane drop ($\bar{q}_{23} = 1846/2433/2936$ W·m^{-2} for $\xi = 0.2/1.0/5.0\%$).

for pure conduction. Apart from a thermal boundary layer at the evaporation interface 2-3 and a second one at the liquid–liquid interface close to the three-phase contact circle, the heat transferred by convection is much larger than that by conduction. As evaporation advances further, no qualitative change in the heat transfer mechanism takes place, and the isotherm contour plots look very similar to the one shown in Fig. 12 for $\xi = 5\%$.

Fig. 13 shows the distribution of the heat flux (rate of heat flow per unit area) along interface 2-3 for the cases $\xi = 0.2\%$, $\xi = 1\%$ and $\xi = 5\%$. The coordinate s_{23} along the interface is related to the length l_{23} the interface has in a vertical cut. The heat flux is related to its respective average value on the interface. Looking at the case $\xi = 0.2\%$, there is a comparatively large heat flux close to the three-phase contact circle, as expected from the isotherm plot. (The downwards directed peak in this curve at $s_{23}/l_{23} \approx 0.96$ is caused by numerical instabilities and has no physical reason.) Going away from the contact circle and approaching the axis of symmetry, the heat flux decreases considerably. Consequently, most of the evaporation takes place in a rather small area. This changes when convective heat transfer becomes more important, as can be seen in Fig. 13 for $\xi = 1\%$ and $\xi = 5\%$. There is still a peak at the contact circle, however, the distribution is much more uniform and near the axis of symmetry the average value is even exceeded. By contrast, the heat flux at the liquid–liquid interface 1-2 (not shown in a figure) is decreasing gradually and reaches a value less than 1% of the average at the axis of symmetry. Obviously, most of the heat transfer across interface 1-2 takes place close to the contact circle. However, only a part of it is conducted directly to the evaporation interface; the rest is removed by the vortex. As a result, the temperature in the rear part of the liquid n-pentane is homogeneously distributed and closer to T_∞ than to T_s. Additionally, evaporation is distributed much more evenly over interface 2-3 than in the early stages when conduction dominates.

The surface-active substances, which are assumed to retard the motion of the liquid–liquid interface in the experiments, have two contrary effects on the heat transfer: On the one hand convective heat transport is weakened, but on the other hand the opening angle θ_2 of the drop's liquid at the three phase contact circle remains smaller and there is a larger region with only a thin film of the dispersed component's liquid between the evaporation interface 2-3 and the surrounding liquid. For the *n*-pentane system it is likely that this second effect exceeds the first one and that this is the reason for the evaporation to proceed faster in the experiment than in the simulation.

5. Conclusions

The finite element method in Lagrangian description enabled the numerical simulation of the direct-contact evaporation of a furan and a *n*-pentane drop in aqueous glycerol. It was not necessary to prescribe the shape of the growing compound drop or to simplify the Navier–Stokes equations considerably. However, the developed code is limited to the case of a rather viscous continuous component, where the problem is physically two-dimensional. The results are in satisfactory agreement with experiments described in the literature. A possible explanation for the discrepancies is the influence of surface-active substances which were present in the experiments but not considered in the simulation. Furthermore, the numerical analysis allowed a more detailed examination of the heat transfer mechanism than experiments.

Acknowledgement

The support of this work by the Deutsche Forschungsgemeinschaft is gratefully acknowledged.

References

[1] G.F. Hewitt, Heat Exchanger Design Handbook, Begell House, 1998.
[2] Y.H. Mori, Classification of configurations of two-phase vapor/liquid bubbles in an immiscible liquid in relation to direct-contact evaporation and condensation processes, Internat. J. Multiphase Flow 11 (4) (1985) 571–576.
[3] P.S. Ayyaswamy, Direct-contact transfer processes with moving liquid droplets, Adv. Heat Transfer 26 (1995) 1–104.
[4] S. Sideman, Y. Taitel, Direct-contact heat transfer with change of phase: Evaporation of drops in an immiscible liquid medium, Internat. J. Heat Mass Transfer 7 (1964) 1273–1289.
[5] M. Song, A. Steiff, P.-M. Weinspach, Direct-contact heat transfer with change of phase: A population balance model, in: Proceedings of the 11th IHTC Kyongju, Korea, Vol. 6, 1998, pp. 457–462.
[6] H.R. Jacobs, Thermal and hydraulic design of direct-contact spray columns for use in extracting heat from geothermal brines, in: F. Kreith, R.F. Boehm (Eds.), Direct-Contact Heat transfer, Hemisphere, Washington, DC, 1988, pp. 343–369.
[7] R.N. Lyon, Direct-contact heat exchangers for OTEC: Some advantages and disadvantages, in: Proceedings of the 8th Ocean Energy Conference, Washington, DC, June 1981, pp. 355–359.
[8] J.D. Wright, Design of direct-contact preheater/boilers for solar pond power plants, in: F. Kreith, R.F. Boehm (Eds.), Direct-Contact Heat Transfer, Hemisphere, Washington, DC, 1988, pp. 299–334.
[9] R.C. Smith, W.M. Rohsenow, M.S. Kazimi, Volumetric heat-transfer coefficients for direct-contact evaporation, ASME J. Heat Transfer 104 (1982) 264–270.
[10] M. Song, A. Steiff, P.-M. Weinspach, Parametric analysis of direct contact evaporation process in a bubble column, Internat. J. Heat Mass Transfer 41 (1998) 1749–1758.
[11] D.H. Klipstein, Heat transfer to a vaporizing immiscible drop, D.Sc. Thesis, Massachusetts Institute of Technology, 1963.
[12] H.C. Simpson, G.C. Beggs, M. Nazir, Evaporation of butane drops in brine, Desalination 15 (1974) 11–23.
[13] Y. Tochitani, Y.H. Mori, K. Komotori, Vaporization of single liquid drops in an immiscible liquid, Part I: Forms and motions of vaporizing drops, Wärme- und Stoffübertragung 10 (1977) 51–59.
[14] Y. Tochitani, T. Nakagawa, Y.H. Mori, K. Komotori, Vaporization of single liquid drops in an immiscible liquid, Part II: Heat transfer characteristics, Wärme- und Stoffübertragung 10 (1977) 71–79.
[15] S.T. Vuong, S.S. Sadhal, Growth and translation of a liquid–vapour compound drop in a second liquid. Part 1: Fluid mechanics, J. Fluid Mech. 209 (1989) 617–637.
[16] S.T. Vuong, S.S. Sadhal, Growth and translation of a liquid–vapour compound drop in a second liquid. Part 2: Heat transfer, J. Fluid Mech. 209 (1989) 639–660.
[17] M.G. Wohak, H. Beer, Numerical simulation of direct-contact evaporation of a drop rising in a hot, less volatile immiscible liquid of higher density—Possibilities and limits of the SOLA-VOF/CSF algorithm, Numer. Heat Transfer A 33 (1998) 561–582.
[18] F. Dammel, Numerische Simulation eines in einer Flüssigkeit aufsteigenden und dabei im Direkt-Kontakt verdampfenden Tropfens, Doctoral Thesis, Technische Universität Darmstadt, 2000, Fortschritt-Berichte VDI, Reihe 3, Nr. 677, VDI Verlag, Düsseldorf, 2001.
[19] M. Wohak, Numerische Simulation des Verdampfungsvorgangs eines aufsteigenden Tropfens im Direkt-Kontakt mit einer heißeren, schwereren und nicht mischbaren Flüssigkeit, Doctoral Thesis, Technische Hochschule Darmstadt, 1995.
[20] J.N. Reddy, D.K. Gartling, The Finite Element Method in Heat Transfer and Fluid Dynamics, CRC Press, Boca Raton, FL, 1994.
[21] F. Dammel, H. Beer, Numerical simulation of the direct-contact evaporation of a drop rising in a second liquid due to buoyancy, in: CD-Rom Proceedings of the European Congress on Computational Methods in Applied Science and Engineering, Barcelona, Spain, 2000.
[22] Y.H. Mori, N. Tsui, M. Kiyomiya, Surface and interfacial tensions and their combined properties in seven binary, immiscible liquid–liquid–vapor systems, J. Chem. Engrg. Data 29 (4) (1984) 407–412.
[23] Y.H. Mori, Private communication, 1994.
[24] R. Clift, J.R. Grace, M.E. Weber, Bubbles, Drops and Particles, Academic Press, New York, 1978.